



# Microstructure and tribological properties of solid lubricant-doped CMT-WAAMed Stellite deposits

Jari Tuominen<sup>1</sup> · Ali Sabr<sup>1</sup> · Leo Hyvärinen<sup>1</sup> · Pasi Peura<sup>1</sup>

Received: 21 January 2024 / Accepted: 22 March 2024  
© The Author(s) 2024

## Abstract

A large share of the world's total energy consumption is used to overcome friction. Therefore, low friction wear-resistant materials are needed. Solid lubricants are solid-phase materials that can reduce friction at different temperatures between two surfaces sliding against each other without the need for a grease or liquid oil medium. In this study, Cold Metal Transfer Wire Arc Additive Manufacturing (CMT-WAAM) was used to deposit solid lubricant ( $WS_2$ ,  $MoS_2$ ,  $CaF_2$ ) doped hypoeutectic Stellite alloy. Fabricated deposits possessed crack- and pore-free microstructures consisting of  $\gamma$ -Co and  $M_7C_3$  carbide eutectics embedded with chromium sulfides and microhardness values of  $\sim 530$  HV<sub>1</sub>. They were also tested in self-mated unidirectional sliding wear tests in dry conditions at room temperature (RT) and at 300 °C in an air atmosphere. The results showed that the dynamic coefficient of friction (COF) decreased  $\sim 27\%$  at RT and  $\sim 21\%$  at 300 °C without losing the wear properties. During sliding wear tests severe strain hardening occurred and  $\gamma$ -Co was found to transform to  $\epsilon$ -Co. The developed deposits can be used as hard facings or 3D printed components in applications that require good sliding wear properties at different temperatures such as metal forming tools, power transmission components, valves, and internal parts of combustion engines.

**Keywords** Wire arc additive manufacturing · Solid lubricant · Stellite · Sliding wear

## 1 Introduction

Approximately 20% of the world's energy consumption is used to overcome friction in transportation, various machinery, and other equipment [1]. By utilizing advanced materials and lubrication techniques, energy losses due to tribology-related issues could be reduced by 40% [1]. Solid lubricants are a group of materials with self-lubricating capability. They are roughly classified according to the operating temperature at which they exhibit the lowest friction. Low temperature ( $< 500$  °C) solid lubricants include, for instance, molybdenum and tungsten disulfides ( $MoS_2$ ,  $WS_2$ ), silver (Ag), and graphite, whereas hexagonal boron nitride (BN) and calcium difluoride ( $CaF_2$ ) constitute the high temperature (HT) ( $> 500$  °C) solid lubricants. Their effect is based on low shear strength and/or high c/a ratio if hexagonal in the crystal structure. Solid lubricant-doped advanced materials are used in applications where

conventional lubricants such as oil and grease do not work due to too high operating temperature, volatilization, sealing problems, production of harmful paste, solidification, and requirements of purity [2–4].

Solid lubricants can be impregnated in various load-carrying metal alloy matrices to decrease friction. The most used method is laser powder cladding a.k.a. laser metal deposition because it is easy to mix different powders. Their embedding as original chemical compounds is, however, difficult because most of them oxidize readily and decompose below the melting temperatures of potential matrix metals. For instance,  $MoS_2$  ( $T_m = 1185$  °C,  $\rho = 5.1$  g/cm<sup>3</sup>) particles ( $< 10$   $\mu$ m) clad with nickel dissociated in pre-placed laser cladding leading to various sulfides with matrix materials, which, nevertheless, possessed low friction [5]. Wolfe et al. [6] managed, however, to embed fine  $< 1$   $\mu$ m  $WS_2$  ( $T_m = 1250$  °C,  $\rho = 7.5$  g/cm<sup>3</sup>) particles together with  $Cr_3C_2$  into Inconel 625 matrix by injecting them to the trailing edge of the melt pool, thus avoiding the direct interaction with the laser beam. Instead of direct injection of solid lubricant particles, Yakovlev et al. [7] fabricated  $MoS_2$  layers by laser cladding the first molybdenum layer, which was later submitted to a heated chamber filled with sulfur vapor. Courant

✉ Jari Tuominen  
jari.tuominen@tuni.fi

<sup>1</sup> Tampere University, Materials Science and Environmental Engineering, 33720 Tampere, Finland

et al. [8] succeeded in leaving graphite ( $T_m = 3675\text{ °C}$ ,  $\rho = 2.2\text{ g/cm}^3$ ) inclusions in the Ti matrix by pre-placed pulsed laser cladding technique due to low heat input and high solidification rates. A significant amount of TiC, however, formed as well. Ag ( $T_m = 960\text{ °C}$ ,  $\rho = 10.5\text{ g/cm}^3$ ) was tried as solid lubricant together with  $\text{CaF}_2/\text{BaF}_2$  in multi-material alloy consisting of 20 vol.% Ni20Cr – 50 vol.%  $\text{Cr}_3\text{C}_2$  – 15 vol.% Ag – 15 vol.%  $\text{CaF}_2/\text{BaF}_2$  [9, 10]. Owing to its immiscibility to the NiCr matrix, Ag was segregated to the surface of the coating during solidification. Torres et al. [11] managed to prevent such an escape of Ag from the melt pool by encapsulating the silver with the addition of  $\text{MoS}_2$  and  $\text{WS}_2$ .  $\text{CaF}_2$  ( $T_m = 1418\text{ °C}$ ,  $\rho = 3.2\text{ g/cm}^3$ ) seemed to be stable since it remained in the final microstructure [9, 10]. Similar observations were made by Wang et al. [12], who embedded  $\text{CaF}_2$  in  $\text{Al}_2\text{O}_3$  matrix on  $\text{Al}_2\text{O}_3$  base material. In addition to enhancing sliding contacts,  $\text{CaF}_2$  is an efficient flux and purifier extensively used to increase the fluidity of melt and eliminate gas and impurities [13]. Shehata et al. [14] and Molian and Hualun [15] applied hexagonal BN ( $T_m = 3000\text{ °C}$ ,  $\rho = 2.3\text{ g/cm}^3$ ) to tool steel and Ti, respectively. In both cases, the majority of BN decomposed and formed new hard phases with matrix elements, which led to better wear resistance.

The objective of this study was to fabricate low-friction Stellite deposits with a cost-effective CMT-WAAM process using tailor-made solid lubricant doped cored wires and test their friction and wear performance at room temperature (RT) and  $300\text{ °C}$  in air atmosphere.

## 2 Materials and methods

### 2.1 Materials

The fabrication of the self-lubricating deposits was performed using a robot-guided CMT arc welding process due to its relatively low heat input. The filler material was a tailor-made Stellite 12 cored wire 1.6 mm in diameter doped with a 7.5 wt.%  $40\text{WS}_2$ - $40\text{MoS}_2$ - $20\text{CaF}_2$  designated as Th12G Lub in this study. Reference deposits were fabricated from a commercial Stellite 12 cored wire (Thalit 12G, Corodur Verschleiss-Shutz GmbH, Thale, Germany) 1.2 mm in diameter and tailor-made Thalit 12G Mod 1.6 mm in diameter where the size of W and Cr particles were diminished in the filler inside the cored wire. Angular Cr and W particles inside the tailor-made wires were up to 140 and 80  $\mu\text{m}$  in Th12G Mod and 230 and 120  $\mu\text{m}$  in Th12G Lub in sizes as displayed in Table 1. Representative fillers inside the wires are displayed in Fig. 1a and b. In an earlier study, Cr particles up to 250 and W particles up to 120  $\mu\text{m}$  in size remained unmelted in the CMT process [16]. For that reason, their size was diminished in tailor-made Th12G Mod cored wire. In

**Table 1** Maximum particle sizes of filler inside the cored wire

Cored wire	Type	Cr	W
Th12G Ø1.2 mm	Commercial	250 $\mu\text{m}$	120 $\mu\text{m}$
Th12G Mod Ø1.6 mm	Tailor-made	140 $\mu\text{m}$	80 $\mu\text{m}$
Th12G Lub Ø1.6 mm	Tailor-made	230 $\mu\text{m}$	120 $\mu\text{m}$

general, Stellite 12 is a carbide-type hypoeutectic Co-based hard-facing alloy with moderate hardness provided by carbon and carbide formers. This alloy is claimed to have excellent resistance to abrasion, erosion, cavitation, and severe sliding wear, and it can be used in applications reaching up to  $700\text{ °C}$  [17]. Th12G's chemical composition is presented in Table 2. Besides the elements reported in the analysis certificate, the filler inside the wire contained some Al, F, Na, Ca, and K particles, which are effective arc stabilizers and deoxidizers [18]. Its melting range is  $1225$ – $1280\text{ °C}$ . The sheath thickness of the cored wire was 0.17 mm, and the type of joint was lapped as displayed in Fig. 2. The sheath and internal areas of the Th12G Lub wire were 0.762 and  $1.205\text{ mm}^2$  leaving a lot of space for filler powders inside the wire. Linear masses of the Th12G Mod and Th12G Lub wires were 0.136 and 0.138 g/cm (for comparison, a solid G4Si1 D1.2 mm is 0.085 g/cm) allowing flawless reciprocating wire motion in the CMT process. The substrate was an S355 construction steel with a thickness of 20 mm. Its chemical composition is presented in Table 2.

### 2.2 Deposition

Deposition experiments were conducted with a Fronius CMT Advanced 4000R single wire welding equipment (Fronius International GmbH, Wels, Austria) mounted to an ABB IRB 4600–40/2.55 robot with an ABB IRBPA-750 turntable (ABB, Västerås, Sweden). After extensive deposition experiments to produce low-diluted fusion-bonded single-layer deposits without pores and cracks, the optimized deposition parameters are presented in Table 3.

### 2.3 Characterization

Surfaces of as-welded CMT-WAAMed deposits were examined with an Alicona InfiniteFocus G5 optical 3D measurement sensor (Alicona Imaging GmbH, Graz, Austria). Profiled areas were  $20 \times 20\text{ mm}^2$ . Both optical and scanning electron microscopy (OM and SEM) were used in inspecting the sample cross-sections prepared from the deposits. The optical microscope used was a Leica DM 2500 M (Leica Microsystems GmbH, Wetzlar, Germany), and the SEM was a JEOL JSM-IT500 (Jeol Ltd., Tokyo, Japan) with the energy dispersive X-ray spectroscopy (EDS). Hardness measurements were conducted using a Matsuzawa MMT-XT

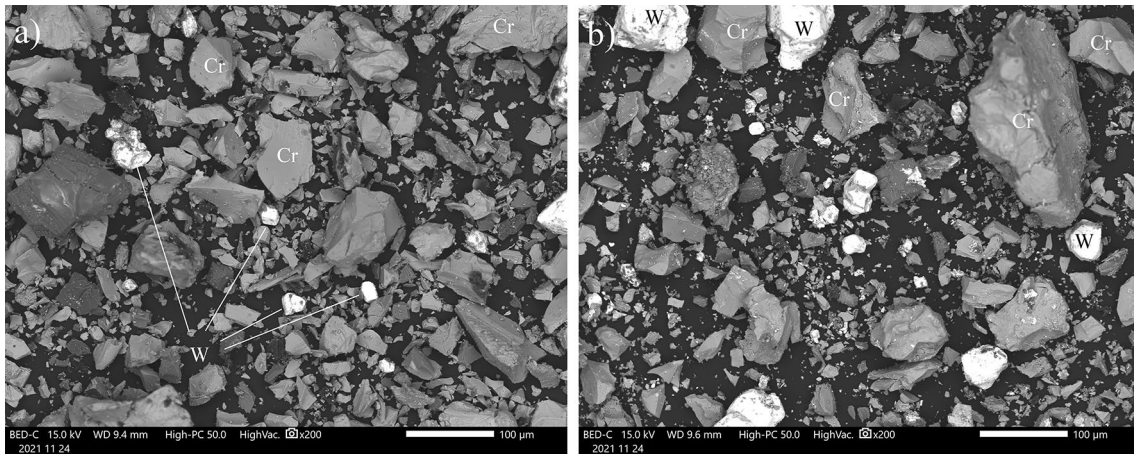


**Fig. 1** Backscattered SEM images of the powders inside the tailor-made **a** Th12G Mod and **b** Th12G Lub cored wires

**Table 2** Chemical compositions of St12 cored wires and S355 substrate in wt.%

Material	Type	C	Mn	Si	Fe	Cr	W	Ni	Co	P	S
Th12G Ø1.2mm <sup>1</sup>	Commercial	1.4	1.0	1.5	<2.5	29.5	8.5	<3.0	Bal		
Th12G Mod Ø1.6 mm	Tailor-made	Diminished W and Cr granulometry									
Th12G Lub Ø1.6 mm	Tailor-made	Doped with 7.5 wt.% (40WS <sub>2</sub> -40MoS <sub>2</sub> -20CaF <sub>2</sub> )									
S355 <sup>2</sup>	Substrate	0.2	1.6	0.6	Bal						

<sup>1</sup>Analysis certificate, <sup>2</sup>Nominal composition

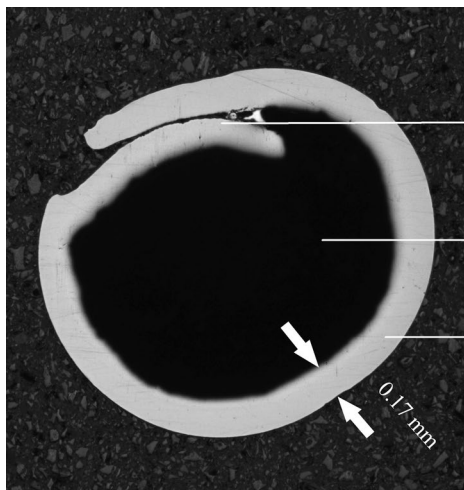


**Fig. 2** Optical microscope image of cross-section of Th12G Lub cored wire 1.6 mm in diameter

(Matsuzawa Co Ltd, Akita, Japan) Vickers microhardness tester. To reveal crystal structures and phases present in deposits, an X-ray diffractometer, Panalytical Empyrean Multipurpose Diffractometer (Malvern Panalytical Ltd, Malvern, UK), was employed using the CoK $\alpha$  radiation at

**Table 3** Optimized CMT-WAAM parameters for St12 cored wires on S355 steel

Parameter	Th12G	Th12G Mod	Th12G Lub
Voltage (V <sub>ave</sub> )	14.7 V	13.5 V	12.6 V
Current (A <sub>ave</sub> )	169 A	180 A	186 A
Arc power (W <sub>ave</sub> )	2484 W	2423 W	2328 W
Travel speed (TS)	3 mm/s	10 mm/s	10 mm/s
Wire feed rate (WFR)	6.5 m/min	3.4 m/min	3.5 m/min
Process gas	Ar + 2CO <sub>2</sub>	Ar + 2CO <sub>2</sub> + 30He	Ar + 2CO <sub>2</sub> + 30He
Process gas flow	15 l/min	15 l/min	15 l/min
Weaving width	16 mm	4 mm	4 mm
Inter-track advance	10 mm	3.5 mm	3.5 mm
Preheat	None	250 °C	250 °C

the voltage of 45 kV and the current of 40 mA. The scanning angle 2 $\theta$  covered a range of 30–90 degrees. Volume fraction quantifications were made with ImageJ software. Analyzed areas were ~2000 × 1300  $\mu\text{m}^2$  for unmelted particles and ~100 × 130  $\mu\text{m}^2$  for sulfides.

## 2.4 Tribology

Self-mated unidirectional sliding wear tests for the parameter-optimized specimens were run to determine their wear behavior under different temperatures and to define the dynamic coefficients of friction (COF). Wear tests were conducted with a pin-on-disc device CETR UMT-2 (Center for Tribology, Campbell, USA). For the wear tests, multiple discs were deposited with the selected alloys, machined to specific dimensions, and test surfaces ground to a  $R_a$  of 0.3–0.4  $\mu\text{m}$ . The disc size was 70 mm in diameter and 10 mm in thickness. The pins were removed from the deposits by wire cutting. The diameter of the rounded pin was 6.35 mm. The radius at the tip of the pin was R20. Figure 3 shows the schematic presentation of the test. Before each test, the wear surfaces of both the disc and the pin were cleaned with ethanol. The weighing was done with a TEOPAL scale (accuracy 0.001 g). The test pieces were weighed five times before and after the tests, and the average was calculated.

The wear tests were performed in dry conditions at RT and 300 °C in an air atmosphere using the normal load of 100N, which gave the maximum Hertzian contact pressure of 907 MPa, a sliding speed of 2400 mm/min, and a testing time of six hours. Repeatability and the accuracy of this test can be evaluated with a coefficient of variation (COV). With the used specimen geometry and the test parameters, COVs for mass loss and COF were 14.2% and 12.5% at RT and 6.9% and 5.5% at 300 °C. According to Ref. [20], a COV of 20% or less for mass loss is a sign of appropriately conducted tests. The worn track on the disc, the worn surface of the pin, and collected wear debris were examined with SEM and Alicona InfineFocus G5 optical measurement system. Electron back-scattered diffraction (EBSD) was used to detect phases in the deformed subsurface of the cross-section of the wear-tested pin. EBSD specimens were polished using a 0.02  $\mu\text{m}$  colloidal silica suspension. The data acquisition for EBSD was done using a Zeiss Ultra

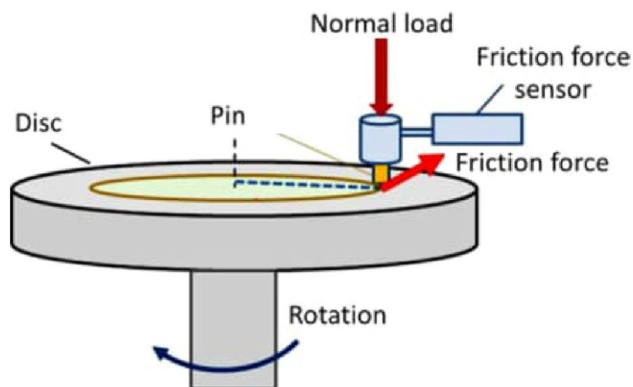


**Fig. 3** Schematic presentation of a pin-on-disc test setup (edited from the Ref. [19])

Plus field emission scanning electron microscope (FESEM) equipped with a Symmetry<sup>®</sup> EBSD detector (Oxford Instruments). The data was acquired with the step size of 0.1  $\mu\text{m}$  over a 70  $\mu\text{m}$   $\times$  45  $\mu\text{m}$  area using an acceleration voltage of 20 kV. The collected data was analyzed using Channel 5 EBSD software.

## 3 Results and discussion

Figure 4a–d shows the surface morphologies of the as-welded CMT-WAAMed deposits. The surface of as-welded Th12G Mod is rather smooth and clean without heavy oxidation as depicted in Figs. 4a and c. The surface of as-welded Th12G Lub is slightly darker and more uneven than Th12G Mod characterized by dark slag islands as shown in Figs. 4b and d. Bright circular spots are regions from where the slag has peeled off. According to EDS analyses, the slag consisted mainly of Ca, Si, Al, and O suggesting that  $\text{CaF}_2$  was intended to be used as HT solid lubricant segregated out of the melt pool. This result contradicts the results presented in Refs. [21, 22], where  $\text{CaF}_2$  was found in the Stellite coatings fabricated by the PTA and pulsed Nd:YAG laser cladding methods. PTA and pulsed Nd:YAG laser cladding processes may have induced higher solidification rates than CMT welding with a preheat of 250 °C used in this study leaving less time for calcium to float away from the melt pool. Generally, such a segregation takes place in welding when there is a low solubility of element A in element B leading to two immiscible liquid phases. According to the Co–Ca binary alloy phase diagram, cobalt solutes at least 10 wt. % of calcium, which disproves the immiscibility theory [23]. Therefore, the calcium may have formed an insoluble compound with Si, Al, and O that floated away from the melt pool. Or it just floated and escaped from the melt pool because  $\text{CaF}_2$  ( $\rho = 3.2 \text{ g/cm}^3$ ) has a much lower density than Stellite 12 ( $\rho = 8.5 \text{ g/cm}^3$ ). The formation of slag from the melt pool was made visible by photographing with a high-speed video camera (Photron FASTCAM SA5, Photron Ltd, Tokyo, Japan) simultaneously illuminating the melt pool with a laser beam (Cavilux, Cavitar Ltd, Tampere, Finland). The sequence of images taken from the video footage is shown in Fig. 5 revealing also the melt pool length, which is estimated to be ~ 17 mm.

### 3.1 Microstructure

The low-magnification SEM images of the cross-sections of Stellite deposits manufactured with process parameters given in Table 3 are illustrated in Figs. 6a and b. Th12G was characterized already in Ref. [16]. In machined conditions, the thicknesses of the deposits are 1.8 mm for Th12G

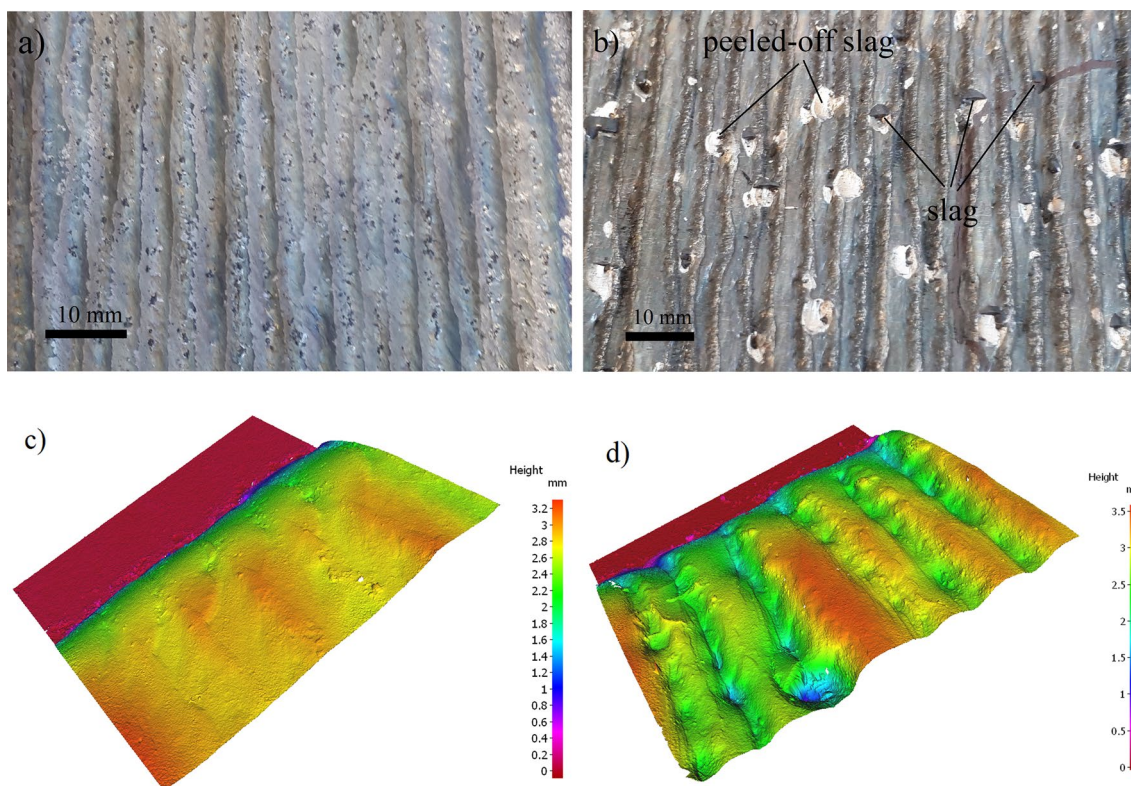


**Fig. 4** Surface morphologies of as-welded CMT-WAAMED Stellite deposits **a, c)** Th12G Mod and **b, d)** Th12G Lub obtained by digital camera (**a, b**) and optical surface profiler (**c, d**)

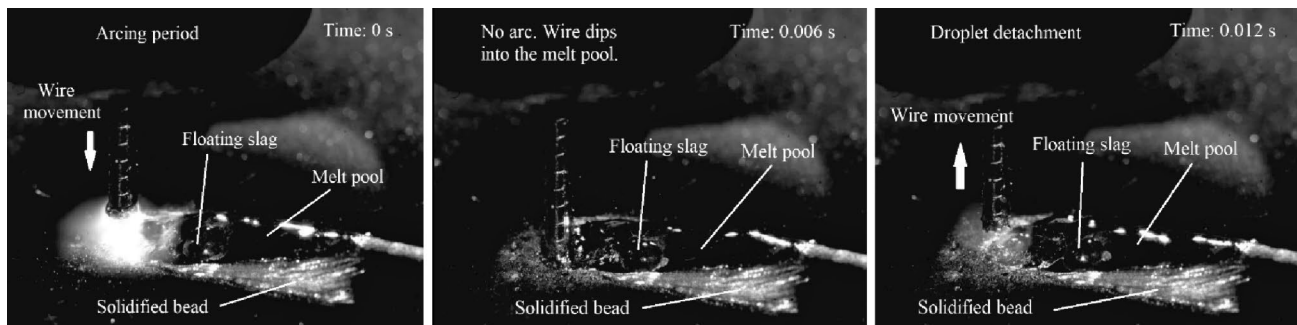


**Fig. 5** Sequence of images taken from video footage of Th12G Lub showing the floating slag on the melt pool during different phases of the CMT cycle. Diameter of the wire is 1.6 mm

Mod and 1.3 mm for Th12G Lub. The deposits are free from cracks and pores. Relatively large bright and dark particles seen on the deposit cross-sections are unmelted powder particles inside the cored wire. The bright particles in Figs. 6a and b are 100 wt. % tungsten and the dark particles are 100 wt. % chromium and 100 wt.% chromium carbides.

According to image analysis, unmelted W content in the Th12G Mod was  $1.4 \pm 0.3$  vol.% averaging  $47 \pm 11$   $\mu\text{m}$  in diameter, and in the Th12G Lub,  $0.7 \pm 0.1$  vol.% averaging  $53 \pm 13$   $\mu\text{m}$  in diameter. The amount of unmelted tungsten particles is lower in Th12G Lub than in Th12G Mod because

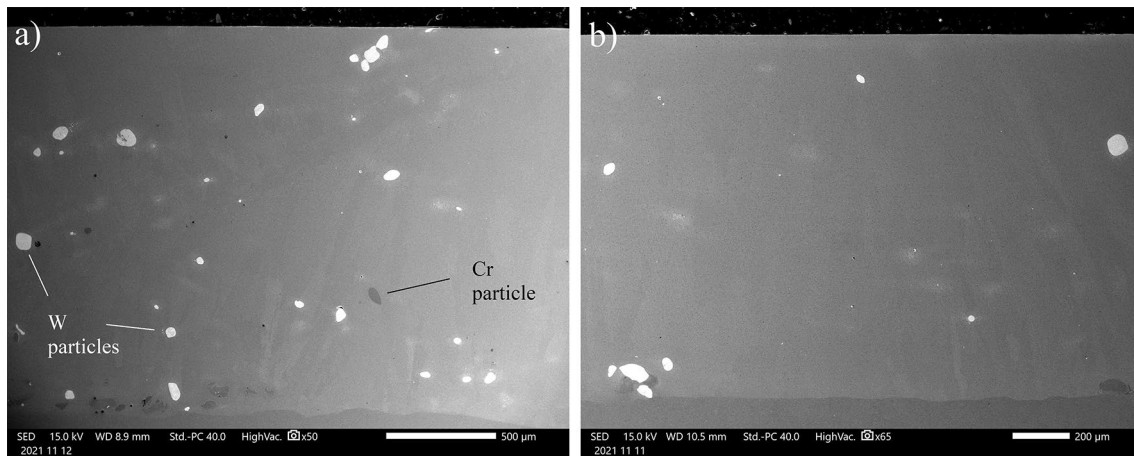


**Fig. 6** Low magnification secondary electron SEM images of cross-sections of CMT-WAAMed Stellite deposits **a** Th12G Mod and **b** Th12G Lub

**Table 4** Average sizes and volume fractions of unmelted W particles in the CMT-WAAMed deposits

Deposit	Wire type	W ( $\mu\text{m}$ )	W (vol.%)
Th12G	Commercial	70	1.7
Th12G Mod	Tailor-made	47	1.4
Th12G Lub	Tailor-made	53	0.7

Th12G Lub includes less Co-based Stellite than Th12G Mod due to solid lubricant addition. Average sizes of the tungsten particles show the benefit of decreased filler granulometry inside the cored wire. The amount of unmelted chromium and chromium carbide particles was far less than W particles because of their lower melting point (Cr:  $T_m$  1907 °C,  $\text{Cr}_3\text{C}_2$ :  $T_m$  ~1800 °C, W:  $T_m$  3422 °C). The measured unmelted particle contents and sizes tabulated in Table 4 are lower than the ones detected earlier from the Th12G [16] showing the positive effect of redesigning the wires with diminished powder granulometry. However, the most ideal situation would be one where no unmelted particles would remain in the structure. The particle size of fillers should be further reduced.

The representative high-magnification SEM images of the cross-sections of Stellite deposits are illustrated in Figs. 7a–d. Both deposits exhibit a well-known structure of hypoeutectic Stellite, which consists of interdendritic regions of a lamellar mixture of the solid solution and eutectic carbides, and the Co-rich dendrites. This was confirmed by taking EDS elemental maps from the deposit to see how the elements solidify and segregate as displayed in Fig. 8.

The chromium is higher in the interdendritic zone, whereas the cobalt content is higher in the dendrites. Although carbon is a problematic element for EDS and its quantity cannot be accurately measured, the results indicated that the carbon tends to be located in the interdendritic zone; the carbon peaks are higher there than in the dendritic zones indicating the formation of carbides with chromium and tungsten. According to image analysis, interdendritic regions occupy ~39 vol.% of the deposit in Th12G Mod and ~44 vol.% in Th12G Lub, which are in good agreement with Refs. [16, 24]. The bright areas in the interdendritic regions shown in Fig. 7b and d are rich in tungsten. Some tiny black dots seen in the interdendritic regions are aluminum oxides with traces of Ca, K, F, and Na. The most striking feature between Th12G Mod and Th12G Lub is the number of black areas in the interdendritic regions. Large amounts of black regions in Th12G Lub are sulfides. According to image analysis, the volume fraction of sulfides in the solid lubricant-doped deposit is 2.5%. EDS elemental maps suggest them to be chromium sulfides. This is in good agreement with Torres et al., who identified chromium sulfides to be  $\text{Cr}_3\text{S}_4$  [11]. Assuming the sulfides to be  $\text{Cr}_3\text{S}_4$  ( $\rho = 4.30 \text{ g/cm}^3$ ) or  $\text{Cr}_2\text{S}_3$  ( $\rho = 3.77 \text{ g/cm}^3$ ), sulfide content in the deposit is 1.1–1.3 wt.%, which is much less than the original solid lubricant content in the Th12G Lub wire.

The chemical compositions throughout the deposits were obtained with EDS area analyses. The analyzed areas were ~40  $\mu\text{m}$  in diameter and they were taken at 200  $\mu\text{m}$  intervals as shown in Fig. 9. The average iron concentrations were  $4.8 \pm 0.3 \text{ wt.}\%$  in the Th12G Mod and  $6.5 \pm 0.5 \text{ wt.}\%$  in the Th12G Lub, which indicates very low chemical

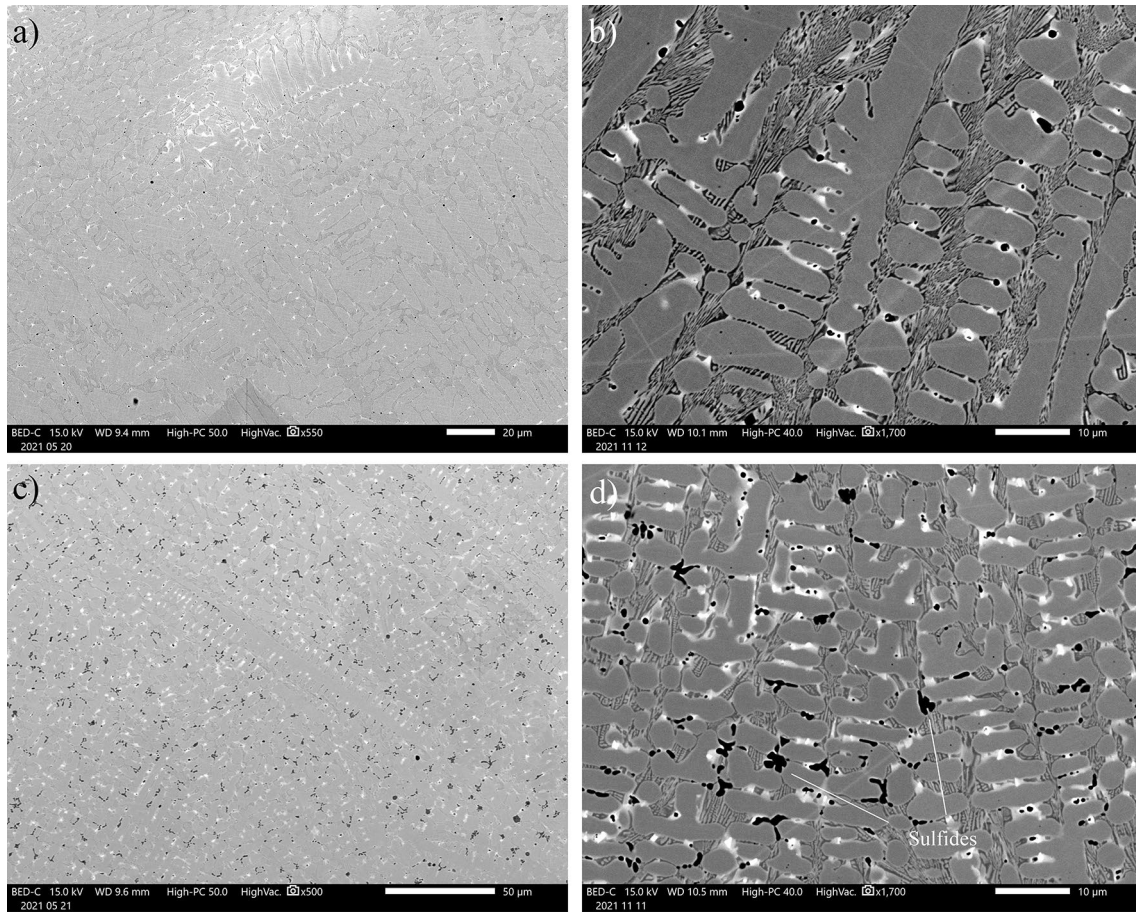


**Fig. 7** High magnification back-scattered electron (BSE) SEM images of cross-sections of CMT-WAAMed Stellite deposits **a, b** Th12G Mod and **c, d** Th12G Lub

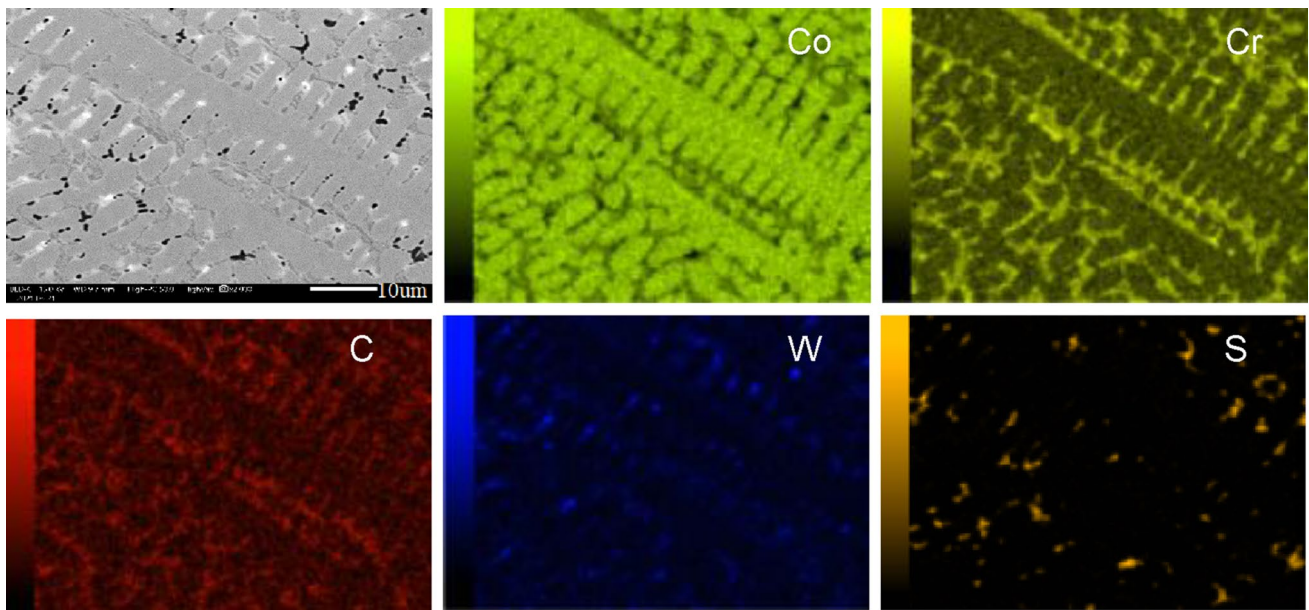


**Fig. 8** EDS elemental maps taken from the cross-section of CMT-WAAMed Th12G Lub deposit

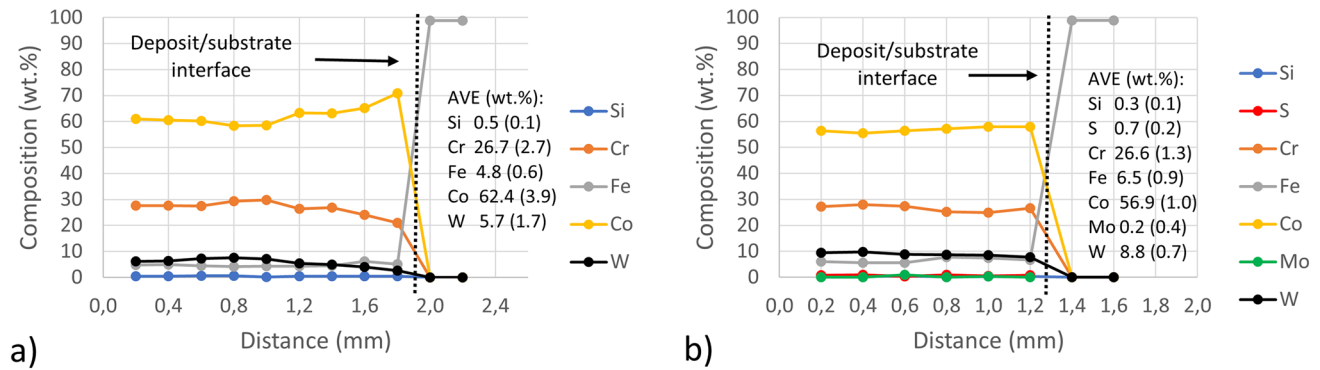


**Fig. 9** EDS composition profile through the depth of a) Th12G Mod and b) Th12G Lub deposits together with average chemical compositions in wt.%. Standard deviations are given in parentheses

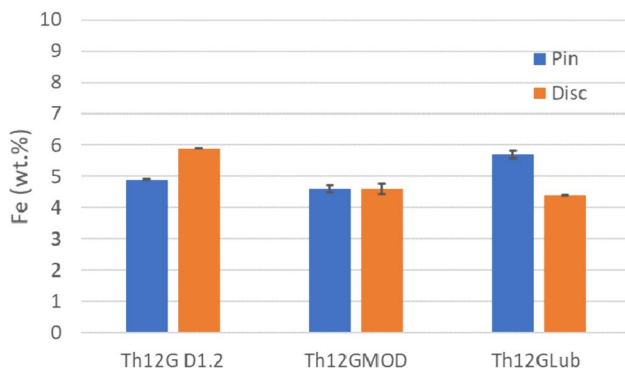


**Fig. 10** EDS area analyses taken from the surfaces of discs and pins

dilution. Intermixed irons are also homogeneously distributed across the cross-section, which indicates good corrosion performance. The amount of tungsten (~5.7 wt.% for Th12G Mod, ~8.8 wt.% for Th12G Lub) and chromium

(~26.7 wt.% for Th12G Mod, ~26.6 wt.% for Th12G Lub) in the matrix are higher than reported earlier for Th12G [16] showing that higher amount of W and Cr is now melting and dissolving in the matrix due to decreased filler granulometry inside the wire and addition of WS<sub>2</sub>.

EDS measurements were also taken from the surfaces of ground discs and pins before subjecting them to wear tests. Fe contents were around 4–6 wt.% as shown in Fig. 10 indicating negligible dilution.

The secondary dendrite arm spacings ( $\lambda_2$ ) were measured from the middle of the deposits in height. They were 3–4  $\mu\text{m}$  in both Th12G Mod and Th12G Lub, which are in the same range as previously measured from the Th12G [16] and slightly higher than measured from laser-clad deposit [25], indicating high solidification and cooling rates. The solidification rates can be estimated via equation [26]:

$$\lambda_2 = 32.8 \times \dot{T}^{-\frac{1}{3}}$$

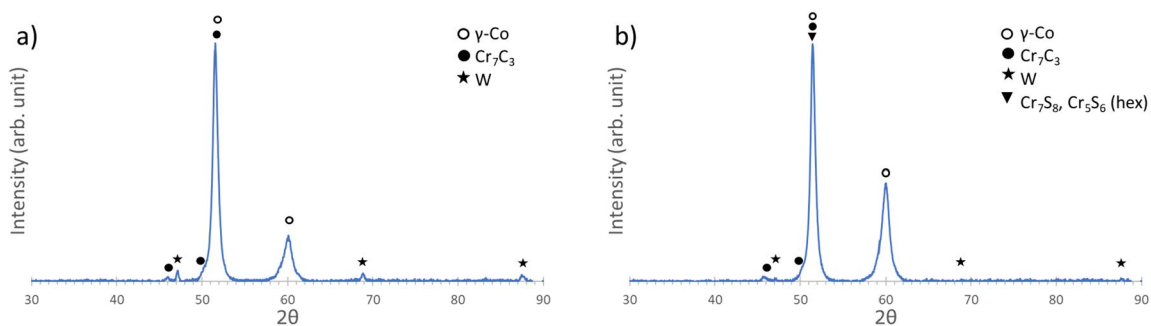


**Fig. 11** XRD patterns of a) Th12G Mod and b) Th12G Lub



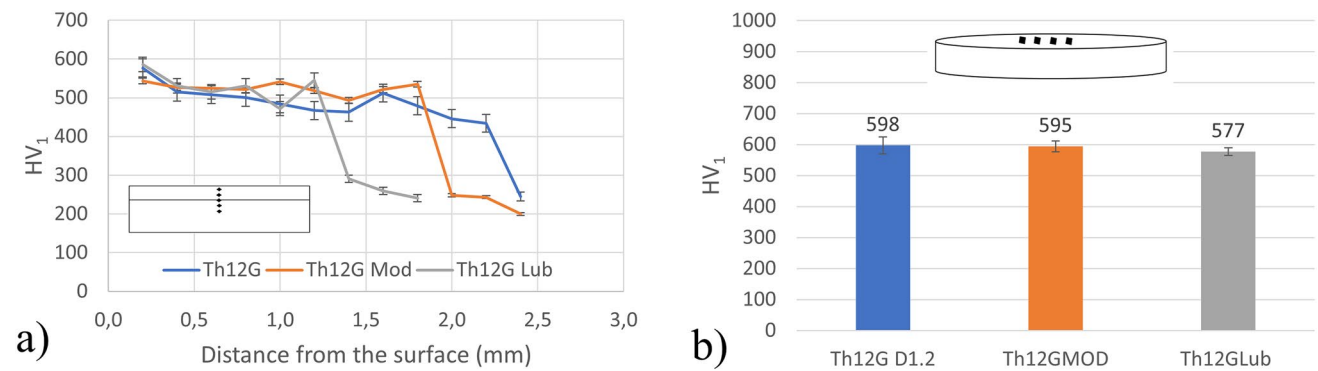


**Fig. 12** Microhardness values of CMT-WAAMed Stellite deposits measured from **a** cross-sections and **b** machined surface of discs

The solidification rate is 600–1400 °C/s. Similar grain sizes and solidification rates can be explained via similar specific energies ( $E = J/mm^2$ ) and welding temperatures. They were 43  $J/mm^2$  for Th12G at RT, 35  $J/mm^2$  for Th12G Mod at 250 °C, and 33  $J/mm^2$  for Th12G Lub at 250 °C. Finer grain structure is known to be beneficial providing higher matrix hardness via grain boundary strengthening as was shown in Ref. [27]. The rate of strain hardening is also known to increase as the microstructure becomes refined [28].

The deposits were also analyzed with XRD to identify the phase compositions. The representative XRD curves taken from the surfaces of the machined wear specimens are illustrated in Fig. 11. The peaks that could be identified were cubic  $\gamma$ -Co (fcc) solid solution, orthorhombic or hexagonal  $M_7C_3$  carbide ( $M = Cr, Co, Fe, W$ ), and cubic tungsten. According to Hou et al. [29],  $M_7C_3$  carbides found from PTA-clad St12 are hexagonal as proved by the TEM studies. It is noteworthy that no  $\epsilon$ -Co (hcp) was observed on the surfaces of the machined wear specimens despite relatively strong work hardening as will be shown below. Chromium sulfides could not be identified either because the largest (100% intensity) peaks overlap with the largest peak of  $\gamma$ -Co (111). After dissociation of  $WS_2$  and  $MoS_2$  in the melt pool, chromium sulfides present a higher stability, i.e. a lower Gibbs free energy of formation particularly at higher temperatures ( $> 750$  °C) than, for instance,  $MoS_2$  [30, 31]. Therefore, the reactions  $MoS_2 + Cr \rightarrow Mo + CrS$  and  $WS_2 + Cr \rightarrow W + CrS$  are more likely to occur, which explains the findings earlier in this study and Refs [11, 32].

### 3.2 Microhardness

Microhardness measurements were performed to study the mechanical properties of the clads. Microhardness profiles

are presented in Fig. 12a. The average microhardness values of the clads are 490 HV<sub>1</sub> for Th12G, 525 HV<sub>1</sub> for Th12G Mod, and 530 HV<sub>1</sub> for Th12G Lub. They are like hardness values reported for PTA-clad St12 in Ref. [24] and higher than 429 HV reported for PTA-clad St12 with a dilution of 8.5% [29]. Somewhat higher microhardness values of modified Th12G Mod and Th12G Lub compared with original Th12G can be attributed to the lower amount of unmelted W and Cr particles and higher amount of W in Th12G Lub due to solid lubricant addition. The hardness increase is based on tungsten's and chromium's effect on carbide formation and solid solution strengthening. W and Cr are also important elements in diminishing the stacking fault energy (SFE) and promoting the work hardening and related  $\gamma$ -Co (fcc)  $\rightarrow$   $\epsilon$ -Co (hcp) phase transformation, which may enhance the wear resistance by increasing the matrix's ability to work harden. Surface hardness values measured from the surfaces of machined discs showed, however, that there are no issues in the ability to work harden when compared to Th12Mod and Th12GLub (Fig. 12b). Owing to machining-induced work hardening, hardness increases were 18% for Th12G, 13% for Th12GMod, and 13% for Th12GLub. The microhardness of the unmelted W and  $Cr_3C_2$  in Th12Mod were 453 HV<sub>0.05</sub> and 2020 HV<sub>0.05</sub>, respectively. Th12GLub also contained some unmelted Cr. Microhardness values were 463 HV<sub>0.05</sub> for W, 2134 HV<sub>0.05</sub> for  $Cr_3C_2$ , and 219 HV<sub>0.05</sub> for Cr. Values for tungsten and chromium are lower and for chromium carbide significantly higher than the surrounding cobalt matrices ( $\sim 525$ – $530$  HV<sub>1</sub>).

### 3.3 Wear tests

The self-mated sliding wear test results for CMT-WAAMed St12 deposits expressed as mass losses are shown in Figs. 13a and b. The total mass loss increased by 900–1500%

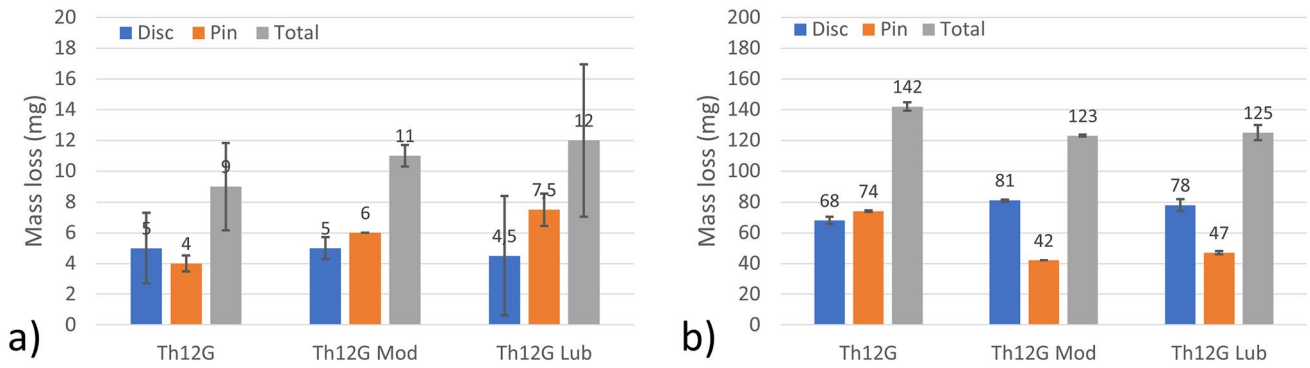


**Fig. 13** Sliding wear test results for the self-mated CMT-WAAMed Stellite deposits at **a** RT and **b** 300 °C

**Table 5** Average microhardness values  $HV_{0.3}$  and STDEV (in parentheses) measured from the non-tested and tested surfaces (average of four measurements)

	Non-tested	RT	Increase (%)	300 °C	Increase (%)
Th12G disc	657 (9)	765 (47)	16	853 (46)	30
Th12G Mod disc	635 (25)	807 (13)	27	823 (69)	30
Th12G Lub disc	623 (19)	704 (10)	13	777 (18)	25

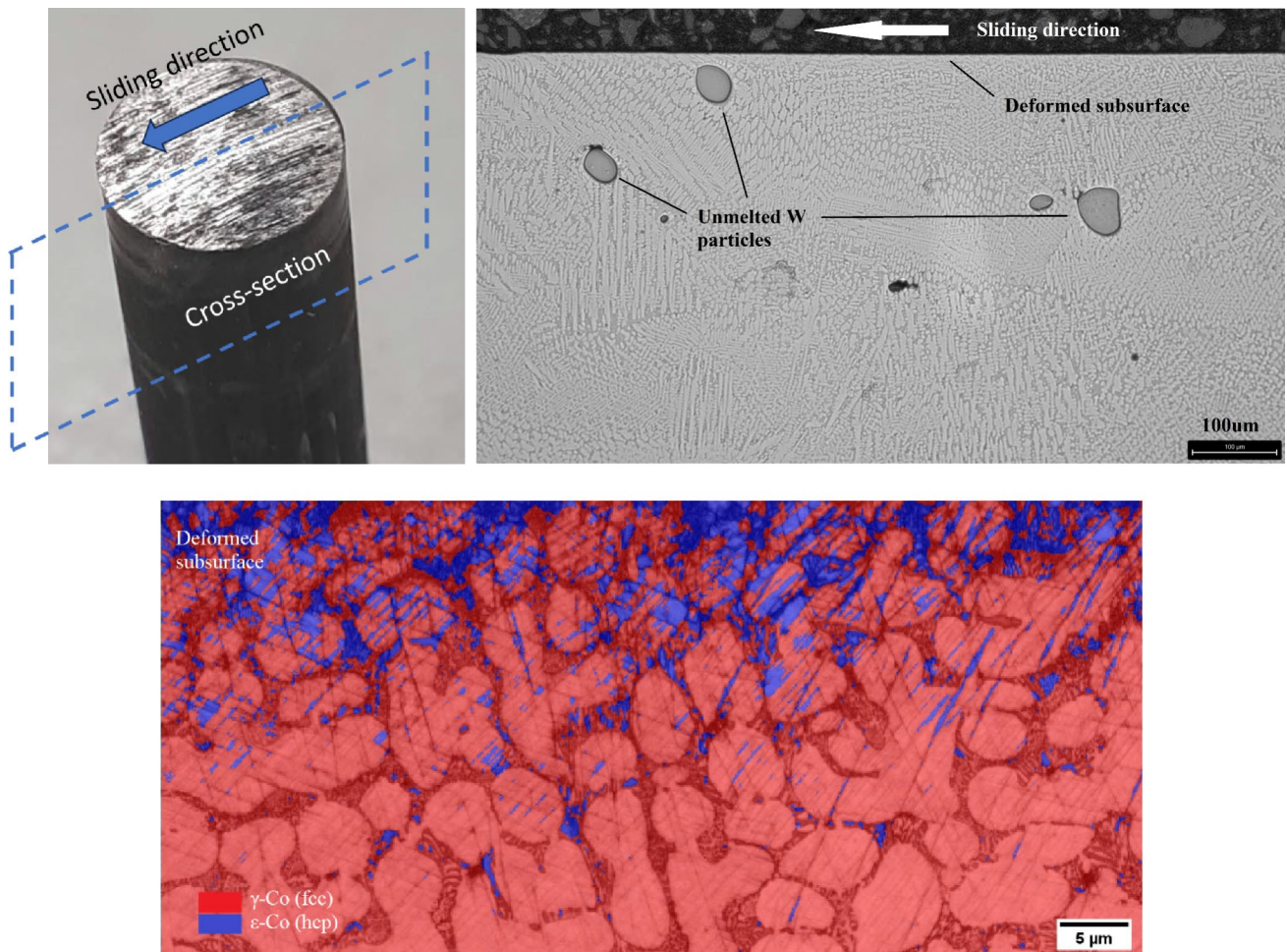


**Fig. 14** High magnification phase color EBSD image of cross-section of tested Th12G Mod pin at RT. Red regions are  $\gamma$ -Co (fcc) and blue regions  $\epsilon$ -Co (hcp)

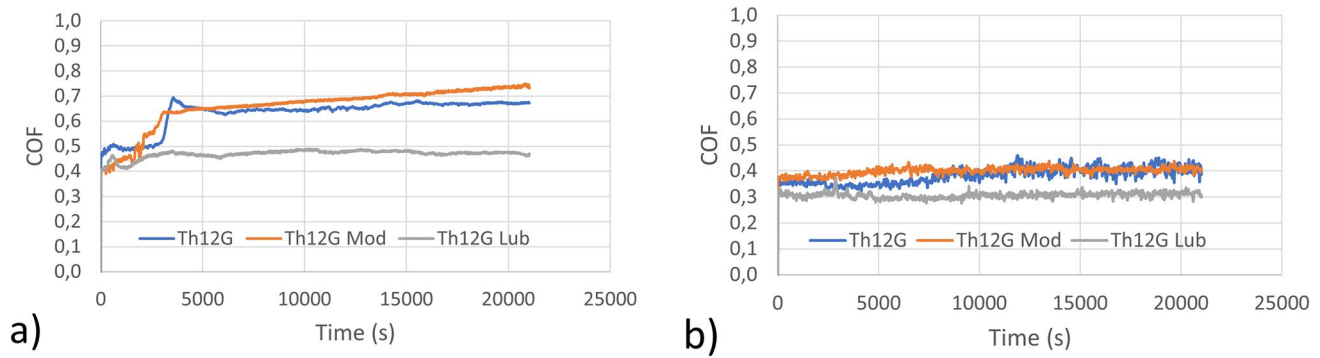


**Fig. 15** COF values as a function of time for self-mated CMT-WAAMed Stellite deposits at a) RT and b) 300 °C

when the temperature was elevated from RT to 300 °C. Wear resistance loss is attributed to the thermal softening of the deposits. Thermal softening was the highest in Th12G which included the largest amount of unmelted tungsten and chromium, which are important carbide formers and solid solution strengtheners. It was also noted that the surface hardness of the disc increased more at 300 °C compared to RT due to strain hardening (Table 5). Hardness growths in the discs at 300 °C and RT were 25–30% and 13–27%, respectively. With the available data, it cannot be said did the different amounts of unmelted tungsten and chromium affect the strain-hardening ability. In theory, tungsten and chromium when dissolved in the solid solution should favor allotropic  $\gamma$ -Co (fcc) to  $\epsilon$ -Co (hcp) transformation and, therefore, promote strain hardening. Such a crystallographic transformation was, indeed, detected from the cross-section of the tested pin by the EBSD analysis. Blue regions near the tested surface are  $\epsilon$ -Co (hcp) as illustrated in Fig. 14. The depth of the deformed zone is  $\sim 20 \mu\text{m}$ . Since the  $\epsilon$ -Co possesses fewer slip systems than  $\gamma$ -Co, the dislocation movement in the  $\epsilon$ -Co is impeded, which resists the plastic deformation and enhances the wear resistance [33]. On the other hand, if  $\{0001\}$  basal planes in  $\epsilon$ -Co orient parallel to the surface of the wear track, friction decreases due to low shear strength [34]. The most important finding in the results is, however, that the addition of solid lubricants did not reduce the wear resistance of the deposits at either test temperature.

The dynamic COF values as a function of test time are presented in Figs. 15a and b. The COFs at 300 °C are significantly lower than the COFs at RT. The average COFs for non-lubricant deposits are 0.63–0.66 at RT and 0.38–0.40 at 300 °C. Therefore, there is a 37–42% decrease in friction due to increased temperature. In solid lubricant-doped deposits,

the effect of temperature increase is not so severe. There is only a 34% decrease in friction due to increased temperature. The effect of temperature on friction can be attributed to the (1) oxidation of specimen surfaces and (2) decreased shear strength of the deposits due to thermal softening.

The effect of solid lubricant at RT is evident. The average COF dropped 25–29% due to solid lubricant additions. The effect at elevated temperature was not so severe. The average COF dropped 18–23% at 300 °C due to solid lubricant additions. This will be explained by the closer examination of wear scars in the coming sections.

### 3.3.1 Wear scars

In general, the observation of the worn surfaces showed long scratches and smooth wear grooves parallel to the sliding direction in all the tested materials as illustrated in Fig. 16. The grooves were created by the detached wear debris, which changed the tribosystem from a 2-body sliding wear to more 3-body abrasion wear. Detached wear debris was probably strongly oxidized and strain-hardened neatly cutting away the material by micro-cutting. Higher magnification SEM images displayed in Fig. 17 show that there is strong oxide formation on the surfaces tested at 300 °C. These oxide layers consist probably of  $\text{CoO}$ ,  $\text{Co}_3\text{O}_4$ , and  $\text{Cr}_2\text{O}_3$  as identified in Ref. [24]. Oxide formation explains the lower effect of solid lubricants on friction at elevated temperatures because there was less metal-to-metal contact at 300 °C than at RT. Another finding is that there are strong signs of plastic deformation and adhered wear debris on the surfaces tested at elevated temperatures because of thermal softening. Slight oxidation was detected on the surface of Th12GMod tested at RT whereas Th12GLub was free from

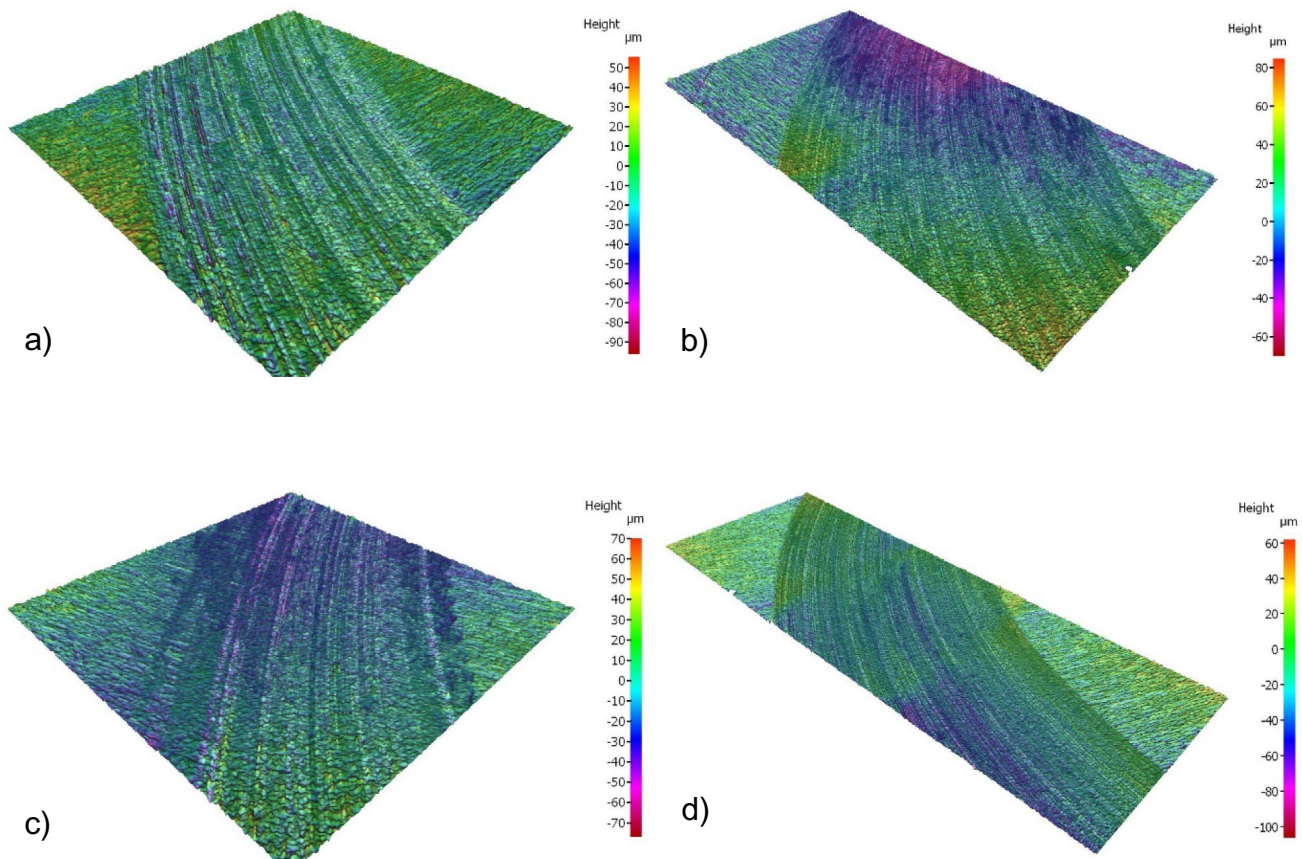


**Fig. 16** Surface profiles of wear scars of the discs **a** Th12G Mod tested at RT, **b** Th12G Mod tested at 300 °C, **c** Th12G Lub tested at RT, and **d** Th12G Lub tested at 300 °C

oxidation as shown in Figs. 17a and c. The temperature between the surfaces caused by the friction was obviously lower in the surfaces doped with solid lubricants. According to the operation principle of sulfides, they are supposed to spread along the mating surfaces due to sliding contact. Such a spreading was not, however, detected with the SEM and EDS.

### 3.3.2 Wear debris

Different amounts of wear debris were collected from the surfaces of the discs after the sliding wear tests. The amount of wear debris was smaller after the tests at RT than at 300 °C. This is consistent with the mass loss results. As displayed in Fig. 18, the wear debris consisted of fine particles and larger platelets up to 160 μm in length in all the cases, and no striking differences were detected between tested materials and temperatures. Such platelets detach from the

materials when the adhesive forces at the junctions between the disc and the pin are stronger than the cohesive strength of the Stellite alloy. According to delamination theory, there is also fatigue cycling involved in the formation of such plate-like wear particles, which are typical in severe wear regimes [35, 36]. Rotating discs inevitably underwent such fatigue cycling.

### 3.4 Future work

The results obtained suggest that solid lubricant content could be further increased in this alloy because the current amount of 7.5 wt.% did not soften the deposit or impair the wear resistance. The role of CaF<sub>2</sub> could be questioned because it floated away from the melt pool and did not remain in the structure. Therefore, it could be replaced by the sulfides or some other solid lubricants. Eventually, the maximum amount of solid lubricants in the cored wire is

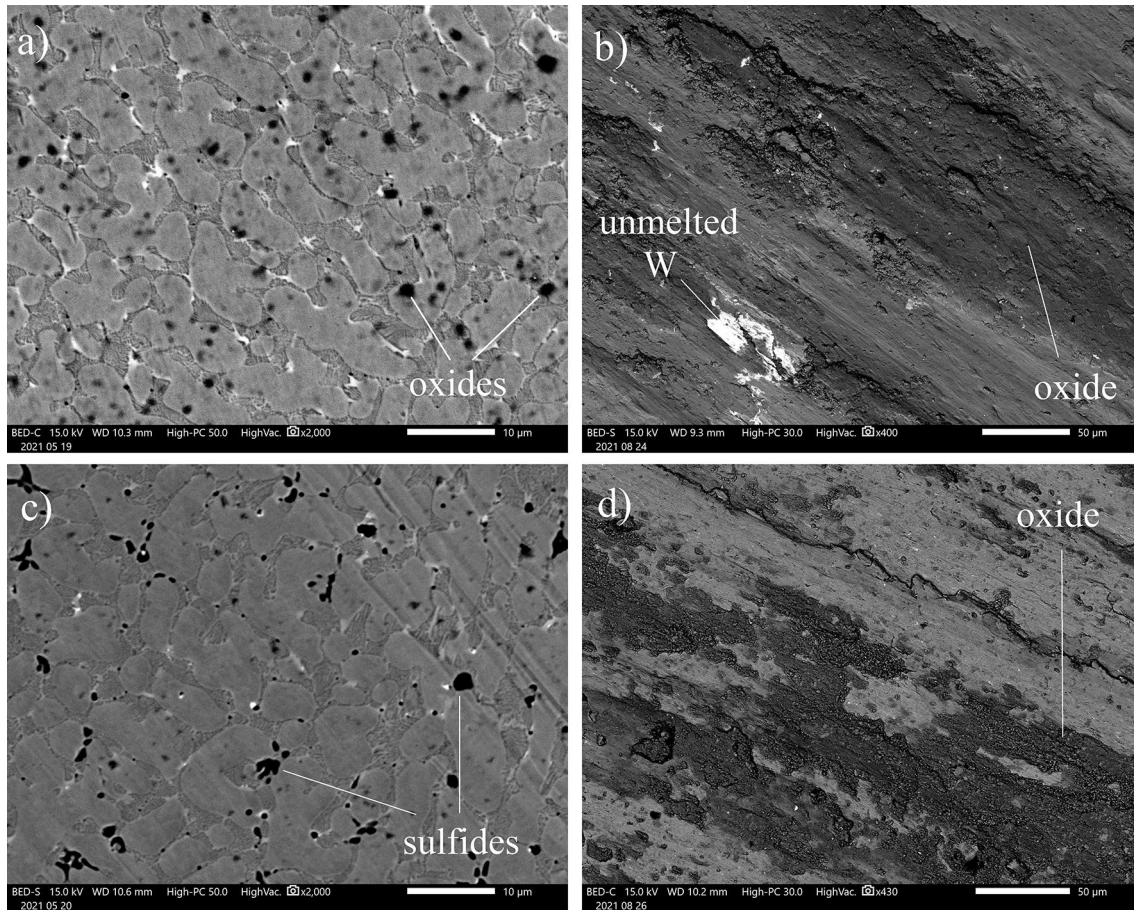


**Fig. 17** BSE SEM micrographs showing the characteristics morphologies of the wear scar of the pins: **a** Th12G Mod tested at RT, **b** Th12G Mod tested at 300 °C, **c** Th12G Lub tested at RT, and **d** Th12G Lub tested at 300 °C

limited by the internal powder-carrying volume inside the wire.

#### 4 Conclusions

The objective of this study was, for the first time, to fabricate low-friction Co-based Stellite deposits with a cost-efficient CMT-WAAM process using a tailor-made solid lubricant ( $\text{MoS}_2$ ,  $\text{WS}_2$ ,  $\text{CaF}_2$ ) doped cored wire and examine their tribological performance in self-mated unidirectional sliding wear tests at RT and 300 °C. The following conclusions can be drawn.

Pore- and crack-free deposits consist of  $\gamma\text{-Co}$  and  $\text{M}_7\text{C}_3$  carbide eutectics embedded with 2.5 vol.% of chromium sulfides. The deposits possess microhardness values of  $\sim 530 \text{ HV}_1$ .

Dynamic COF decreases  $\sim 27\%$  at RT and  $\sim 21\%$  at 300 °C without losing the wear properties compared to non-lubricant doped Stellite deposit. The influence of sulfides is higher at RT than at elevated temperatures because there is more metal-to-metal contact at RT. Large oxide layers are developed on the mating wear scars during the tests at 300 °C.

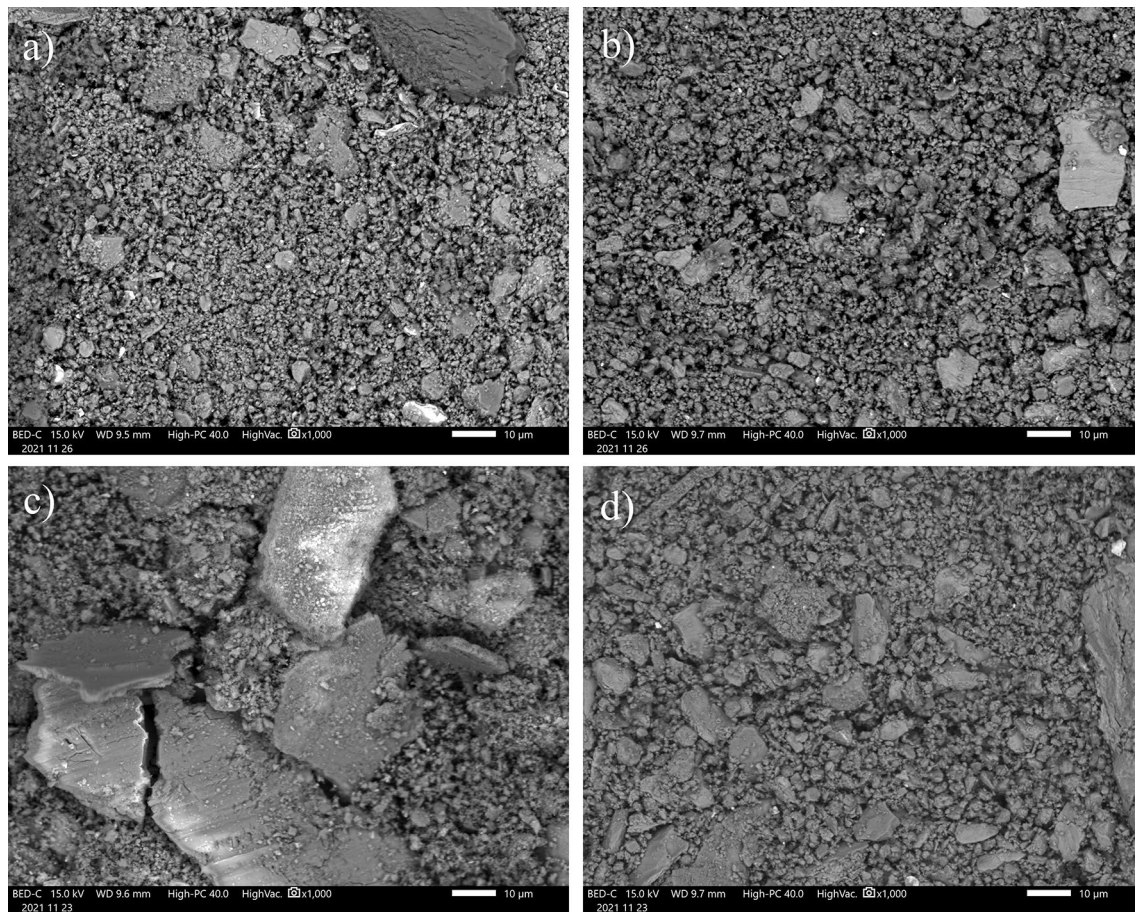


**Fig. 18** BSE SEM micrographs showing the characteristics morphologies of the wear debris: **a** Th12G Mod tested at RT, **b** Th12G Mod tested at 300 °C, **c** Th12G Lub tested at RT, and **d** Th12G Lub tested at 300 °C

Significant hardness increase (~ 15–30%) and strain hardening associated with  $\gamma$ -Co (fcc) to  $\epsilon$ -Co (hcp) transformation takes place during the wear tests.

The tribological performance of deposits could be further enhanced by increasing the sulfide content above 2.5 vol.% and decreasing the size of high melting point tungsten and chromium particles below 80  $\mu\text{m}$  for the tungsten and 140  $\mu\text{m}$  for the chromium in the filler inside the cored wire.

**Acknowledgements** This research was carried out as part of the ‘CINEMA – Towards circular economy via ecodesign and sustainable remanufacturing’ and ‘CASEMATE – Computationally aided systems engineering for marine advanced technology for the environment’ projects. The work has been made possible by financial support from the European Regional Development Fund (European Interreg North 2014–2020) and Business Finland.

**Funding** Open access funding provided by Tampere University (including Tampere University Hospital).

**Data availability** Data available on request from the authors.

## Declarations

**Conflict of interest** The authors declare that they have no known competing financial interests or personal relationships that could have appeared to influence the work reported in this paper.

**Open Access** This article is licensed under a Creative Commons Attribution 4.0 International License, which permits use, sharing, adaptation, distribution and reproduction in any medium or format, as long as you give appropriate credit to the original author(s) and the source, provide a link to the Creative Commons licence, and indicate if changes were made. The images or other third party material in this article are included in the article’s Creative Commons licence, unless indicated otherwise in a credit line to the material. If material is not included in the article’s Creative Commons licence and your intended use is not permitted by statutory regulation or exceeds the permitted use, you will need to obtain permission directly from the copyright holder. To view a copy of this licence, visit <http://creativecommons.org/licenses/by/4.0/>.

## References

1. Holmberg K, Erdemir A (2017) Influence of tribology on global energy consumption, costs and emissions. *Friction* 5:263–284. <https://doi.org/10.1007/s40544-017-0183-5>

2. Quazi MM, Fazal MA, Haseeb ASMA, Yusof F, Masjuki HH, Arslan A (2016) A review of the laser cladding of self-lubricating composite coatings. *Lasers Manuf Mater Process* 3:67–99. <https://doi.org/10.1007/s40516-016-0025-8>
3. Miyoshi K (2007) Solid lubricants and coatings for extreme environments: state-of-the art survey. *NASA/TM-2007-214668*, 1–16.
4. Aouadi SM, Gao H, Martini A, Scharf TW, Muratore C (2014) Lubricious oxide coatings for extreme temperature applications: a review. *Surf Coat Technol* 257:266–277. <https://doi.org/10.1016/j.surfcoat.2014.05.064>
5. Xu J, Liu W, Zhong M (2006) Microstructure and dry sliding wear behavior of MoS<sub>2</sub>/TiC/Ni composite coatings prepared by laser cladding. *Surf Coat Technol* 200:4227–4232. <https://doi.org/10.1016/j.surfcoat.2005.01.036>
6. Wolfe DE, Singh J, Senderson JS, Zabinski J (2000) Laser-clad composite coatings. *Adv Mater* 158:41–44
7. Yakovlev A, Bertrand P, Smurov I (2004) Wear-resistant coatings with engineered structure by laser cladding. *Tribol Lett* 17:705–708. <https://doi.org/10.1007/s11249-004-8076-y>
8. Courant B, Hantzpergue JJ, Benayoun S (1999) Surface treatment of titanium by laser irradiation to improve resistance to dry-sliding friction. *Wear* 236:39–46. [https://doi.org/10.1016/S0043-1648\(99\)00254-9](https://doi.org/10.1016/S0043-1648(99)00254-9)
9. Liu XB, Wang CM, Yu LG, Wang HM (1999) Microstructure of laser clad high-temperature self-lubricating wear-resistant composite coating. *Proc SPIE* 3862:423–427
10. Liu XB, Wang CM, Yu LG, Wang HM (2000) Laser cladding for high-temperature self-lubricating wear-resistant composite coatings on  $\gamma$ -TiAl intermetallic alloy Ti-48Al-2Cr-2Nb. *Proc SPIE* 3888:312–317
11. Torres H, Slawik S, Gachot C, Prakash B, Rodriguez Ripoll M (2018) Microstructural design of self-lubricating laser claddings for use in high temperature sliding applications. *Surf Coat Technol* 337:24–34. <https://doi.org/10.1016/j.surfcoat.2017.12.060>
12. Wang HM, Yu YL, Li SQ (2002) Microstructure and tribological properties of laser clad CaF<sub>2</sub>/Al<sub>2</sub>O<sub>3</sub> self-lubricating wear-resistant ceramic matrix composite coatings. *Scr Mater* 47:57–61. [https://doi.org/10.1016/S1359-6462\(02\)00086-6](https://doi.org/10.1016/S1359-6462(02)00086-6)
13. Yang S, Chen N, Liu W, Zhong M, Wang Z, Kokawa H (2004) Fabrication of nickel composite coatings reinforced with TiC particles by laser cladding. *Surf Coat Technol* 183:254–260. <https://doi.org/10.1016/j.surfcoat.2003.09.062>
14. Shehata GH, Moussa AMA, Molian PA (1993) Nd:YAG laser alloying of high-speed steel tools with BN and Ti/BN and the effects on turning performance. *Wear* 170:199–210. [https://doi.org/10.1016/0043-1648\(93\)90241-D](https://doi.org/10.1016/0043-1648(93)90241-D)
15. Molian PA, Hualun L (1989) Laser cladding of Ti-6Al-4V with BN for improved wear performance. *Wear* 130:337–352. [https://doi.org/10.1016/0043-1648\(89\)90187-7](https://doi.org/10.1016/0043-1648(89)90187-7)
16. Tapiola J, Tuominen J, Vihinen J, Vuoristo P (2023) Sliding wear behavior of cold metal transfer clad Stellite 12 hardfacings on martensitic stainless steel. *Weld World* 67:573–584. <https://doi.org/10.1007/s40194-022-01390-6>
17. Stellite 12 alloy datasheet. Kennametal Stellite. [http://www.stellite.com/Portals/0/KMT\\_Stellite12\\_DataSheet\\_FINAL.pdf](http://www.stellite.com/Portals/0/KMT_Stellite12_DataSheet_FINAL.pdf). Accessed 18 Aug 2022
18. Guest SD (2014) Depositing Ni-WC wear resistant overlays with hot-wire assist technology. Dissertation, University of Alberta
19. Kandeve M, Kalitchin Z, Zadorozhnaya E, Vencel A (2022) Performance characteristics of lubricant based on rapeseed oil containing different amounts of metal-containing additive. *Ind Lubr Tribol* 74:309–315. <https://doi.org/10.1108/ILT-07-2021-0259>
20. ASTM G99-95a (Reapproved 2000), Standard Test Method for Wear Testing with a Pin-on-Disk Apparatus, Annual Book of ASTM Standards, Vol 03.02., ASTM International, PA, USA, 417–421
21. Baiamonte L, Pulci G, Hlede E, Bartuli C, Valente T, Marra F (2017) Self-lubricating cobalt-based composite coatings deposited by plasma transferred arc. In: *Thermal Spray 2017: Proceedings of the International Thermal Spray Conference*, ASM Thermal Spray Society, Düsseldorf, Germany
22. Yan H, Zhang J, Zhang P, Yu Z, Li C, Xu P, Lu Y (2013) Laser cladding of Co-based alloy/TiC/CaF<sub>2</sub> self-lubricating composite coatings on copper for continuous casting mold. *Surf Coat Technol* 232:362–369. <https://doi.org/10.1016/j.surfcoat.2013.05.036>
23. Massalski TB (1986) Binary alloy phase diagrams, vol 1. American Society for Metals, Metals Park
24. Motallebzahed A, Atar E, Cimenoglu H (2015) Sliding wear characteristics of molybdenum containing Stellite 12 at elevated temperatures. *Tribol Int* 91:40–47. <https://doi.org/10.1016/j.triboint.2015.06.006>
25. Frenk A, Kurz W (1994) Microstructural effects on the sliding wear resistance of a cobalt-based alloy. *Wear* 174:81–91. [https://doi.org/10.1016/0043-1648\(94\)90089-2](https://doi.org/10.1016/0043-1648(94)90089-2)
26. Frenk A, Kurz W (1993) High speed laser cladding: solidification conditions and microstructure of a cobalt-based alloy. *Mater Sci Eng A* 173:339–342. [https://doi.org/10.1016/0921-5093\(93\)90240-F](https://doi.org/10.1016/0921-5093(93)90240-F)
27. Atamert S, Stekly J (1993) Microstructure, wear resistance and stability of cobalt based and alternative Iron based hardfacing alloys. *Surf Eng* 9:231–240. <https://doi.org/10.1179/sur.1993.9.3.231>
28. Atamert S, Bhadeshia HKDH (1989) Comparison of microstructures and abrasive wear properties of Stellite hardfacing alloys deposited by arc welding and laser cladding. *Metall Trans A* 20:1037–1053. <https://doi.org/10.1007/BF02650140>
29. Hou QY, Gao JS, Zhou F (2005) Microstructure and wear characteristics of cobalt-based alloy deposited by plasma transferred arc weld surfacing. *Surf Coat Technol* 194:238–243. <https://doi.org/10.1016/j.surfcoat.2004.07.065>
30. Zeng Y, Domask AC, Mohney SE (2016) Condensed phase diagrams for the metal-W-S systems and their relevance for contacts to WS<sub>2</sub>. *Mater Sci Eng B* 212:78–88. <https://doi.org/10.1016/j.mseb.2016.07.005>
31. Furlan KP, Prates PB, dos Santos TA, Dias MVG, Ferreira HT, Neto JBR, Klein AN (2015) Influence of alloying elements on the sintering thermodynamics, microstructure and properties of Fe-MoS<sub>2</sub> composites. *J Alloys Compd* 652:450–458. <https://doi.org/10.1016/j.jallcom.2015.08.242>
32. Torres H, Vuchkov T, Slawik TS, Gachot C, Prakash B, Ripoll MR (2018) Self-lubricated laser claddings for reducing friction and wear from room temperature to 600°C. *Wear* 408–409:22–33. <https://doi.org/10.1016/j.wear.2018.05.001>
33. Yang D, Wang Q, Wei X, Hua C, Qu S, Xu J, Chen J, Yu C, Lu H (2019) Effects of isothermal aging process on microstructure and mechanical properties of Stellite 6 coatings by plasma arc cladding. *Metall Mater Trans* 50A:2807–2816. <https://doi.org/10.1007/s11661-019-05196-y>
34. D.H.E. Persson (2005) On the mechanisms behind the tribological performance of stellites. Dissertation, Uppsala University
35. Arnell RD, Davies PB, Halling J, Whomes TL (1991) *Tribology: principles and design applications*. Springer-Verlag, New York
36. Bhansali KJ (1980) Adhesive wear of nickel- and cobalt-base alloys. *Wear* 60:95–110. [https://doi.org/10.1016/0043-1648\(80\)90251-3](https://doi.org/10.1016/0043-1648(80)90251-3)